A Reusable Battery-Free RFID Temperature Sensor

Yousuf Shafiq, *Student Member, IEEE*, John S. Gibson, *Member, IEEE*, Hyun Kim, Cedric P. Ambulo, Taylor H. Ware, and Stavros V. Georgakopoulos, *Senior Member, IEEE*

***Abstract*— A new passive radio frequency identification (RFID) temperature sensor is presented for monitoring the temperature of the surrounding environment of perishable goods, such as foods and medicines, in the cold supply chain. Specifically, this sensor self-tunes between 902 and 928 MHz, operating in the RFID UHF band, as the temperature rises or falls beyond a certain threshold. The novelty of this passive sensor is its ability to operate through multiple high-/low-temperature cycles. The design consists of a planar dipole antenna with a customized integrated T-match network (ITMN) that is actuated above a ground plane. The actuation shifts the operating frequency and is controlled by liquid crystal elastomers (LCEs), which are programmable and reversible temperature-dependent polymers. As a result, our design can be reconfigured to operate at various temperature ranges for which the LCE is designed to operate. The analysis is performed to examine the performance of the proposed sensor near practical items and when it is in close-proximity to an additional sensor with varying orientation. Finally, the sensor's performance was validated through full-wave simulations using ANSYS HFSS and measurements. Both the simulation and measurements agreed well with theory.**

***Index Terms*— 4-D-printed liquid crystal elastomers (LCEs), LCEs, radio frequency identification (RFID), RFID impedance matching, RFID impedance measuring, T-match network (TMN), temperature sensor.**

I. Introduction

A SUBSTANTIAL variety of essential foods and pharmaceuticals must be maintained within a certain temperature range to ensure suitable quality for human consumption [1]–[5] Additionally, 65% of the retail food market consists of fresh-food products [6]. Consequently, due to the safety risk and high consumption rate, temperature monitoring control stages are installed along the cold supply chain. However, these monitoring stations can exist only at discrete locations, such as the refrigerated shipping containers and at sending and receiving checkpoints [1], [5].

These discrete temperature observations are then used to assess the overall condition of the perishable goods [1], [7]. As a result, the temperature conditions due to any problems at intermediate stages are unknown [7]. Common problems that occur in the cold supply-chain include: malfunctioning refrigeration equipment, extended wait-times at the cargo bay, and operator errors [4], [7]. The global sales of organic foods amount to a U.S. $81.6 billion industry [8]. Also, 30% of fresh products are wasted at some point during transit in the cold-supply chain [1]. Accordingly, the temperature sensor proposed in this paper is a cost-effective solution that has the potential to yield large savings in this industry.

Specifically, an enhanced solution to monitoring perishable goods in the cold supply chain is a sensor that has the capability to monitor individual goods independently and continuously. Additionally, the sensor should have a non-line-of-sight communication link capability and operate using passive technology for cost-effectiveness and longevity. This proposed solution would mitigate any uncertainties in regard to the integrity and quality of important foods and medicines because temperature readings can be documented at any time and location.

Radio frequency identification (RFID) technology provides an auspicious platform with a standardized communication protocol that fulfills all the desired sensor attributes mentioned above [9, pp. 42–46]. Currently, RFID tags for temperature monitoring are available [2]. An example of such a tag is the Freshtime Sensor RFID Classic Tag which is a semipassive RFID tag from Infratab [10]. This sensor takes temperature samples and integrates over time to predict the shelf-life of a product. Another example is the i-Q32T from Identec Solutions located in Kristiansand, Norway. This temperature monitoring tag stores temperature readings that can be retrieved from a distance of 100 m [11]. Finally, the IDS-SL13A from IDS Microchip AG is a semipassive temperature datalogger [12]. Although these sensors can provide a suitable form of temperature monitoring, they do not simultaneously meet all the attributes of the proposed solution. Specifically, they are expensive, require batteries, and do not provide real-time readings. Additionally, temperature indicator labels are commonly used to detect temperature threshold crossing of perishable goods as well. However, these labels can detect only a single temperature threshold violation (single-use) and they relay it through a change in color. Therefore, a clear line-of-visibility is required [1]. Hence, monitoring individual packages over large distances in crowded shipping containers is not practical when using such labels.

In this paper, an RFID passive temperature sensor has been designed, fabricated, and tested, which self-tunes between 902 and 928 MHz, operating in the RFID UHF band, as the temperature rises or falls beyond a certain threshold. Specifically, at room temperature, the sensor operates at 902 MHz,

Manuscript received September 8, 2018; revised April 27, 2019; accepted May 16, 2019. Date of publication June 11, 2019; date of current version October 4, 2019. This work was supported by the National Science Foundation under Grant ECCS 1711467. *(Corresponding author: Stavros V. Georgakopoulos.)*

Y. Shafiq and S. V. Georgakopoulos are with the Department of Electrical and Computer Engineering, Florida International University, Miami, FL 33174 USA (e-mail: yshaf001@fiu.edu; georgako@fiu.edu).

J. S. Gibson was with the Department of Electrical and Computer Engineering, Florida International University, Miami, FL 33174 USA. He is now with the Air Force Research Laboratory, Sensors Directorate, Wright Patterson Air Force Base, OH 45433 USA (e-mail: john.gibson.30@us.af.mil).

H. Kim, C. P. Ambulo, and T. H. Ware are with the Bioengineering Department, The University of Texas at Dallas, Richardson, TX 75080 USA (e-mail: kimhyun@utdallas.edu; cedric.ambulo@utdallas.edu; taylor.ware@utdallas.edu).

Color versions of one or more of the figures in this article are available online at http://ieeexplore.ieee.org.

Digital Object Identifier 10.1109/TAP.2019.2921150

and at approximately 160 °C, the sensor operates at 928 MHz. The sensor consists of a planar dipole antenna with a customized matching network that is placed above a ground plane. The shift in the frequency is accomplished by actuating the antenna above the ground plane. A novel, temperature-responsive, 4-D-printed liquid crystal elastomer (LCE) is used for the antenna actuation [13]. The unique property of the LCE is that it changes shape when the temperature is increased and returns to the original relaxed state as the temperature is restored. Moreover, the LCE can be actuated and relaxed through multiple temperature cycles [14], [15]. Hence, the proposed passive sensor can be used to detect multiple temperature threshold violations, as well as multiple returns to normal operating temperatures, thereby providing continuous monitoring of goods. Accordingly, since the developed sensor functions through the exposure of the LCE array to the surrounding elevated temperatures, it is most suitable for the detection of ambient temperature threshold crossings. One envisioned application of the developed sensor is to accompany packages or pallets in the cold-supply-chain to monitor the temperature conditions in cargo transportation containers during the delivery cycle.

The proposed sensor in this paper was designed using currently available 4-D-printed LCE technology with a well-matured fabrication process. Such LCEs react only to elevated temperatures of approximately 160 °C [13], [16]. Thus, the sensor detailed in this paper serves as a proof-of-concept. Most importantly, the physics involved in the shifting of the sensor's operating frequency is independent of the temperature. That is, the operating frequency of the developed sensor depends only on the height of the designed RFID antenna above the ground plane, and the only component that is dependent on the temperature is the selected 4-D-printed LCE array. Therefore, the developed sensor can be adapted to cold environments by replacing the current 4-D-printed LCE array with shape-memory polymers or LCEs that react to lower temperatures to provide temperature threshold detection in the cold-supply chain [17]. However, it should also be noted that the unique advantage of LCEs compared to other shape-memory polymers is their ability to operate reversibly, and they are reusable since they are able to go through many high-/low-temperature-dependent actuation cycles [13], [16]. Our team has developed 4-D-printed heat-responsive LCEs that are used here. Also, we are currently working on developing the fabrication process for LCEs that respond to cold temperatures that could be integrated into our proposed sensing tag.

Finally, to assess the overall performance of the developed sensor, we compare it to a commercially available RFID temperature sensor. The Freshtime Sensor RFID Classic Tag by Infratab is designed for the same application as the sensor proposed in this paper, namely to monitor temperature conditions of perishable items in the cold-supply chain. Table I compares useful technical parameters associated with RFID temperature sensors that are intended for temperature monitoring in the cold-supply chain.

From Table I, it is apparent that our proposed sensor provides an improved form of temperature sensing. Specifically, our sensor provides a battery-free (very long lifetime), cost-effective, real-time, and continuous solution for temperature monitoring.

TABLE I
PERFORMANCE COMPARISON OF THE DEVELOPED SENSOR

Parameter	Developed Sensor in this Research	Freshtime Sensor RFID Classic Tag by Infratab
Technology	Passive (Batter-free)	Semi-Passive (manufacturer battery replacement required/yr.)
Information Delivery	Frequency Domain	Coded Data Stream
Tracking Domain	Real-time	Data-logger
Sensing Functionality	Dynamic antenna control using LCE technology	Separate temperature IC sensor
Frequency of Operation (MHz)	905 and 928	860 – 960
Max Range (m)	1.4	7
Temperature Range	22ºC and 160ºC (Adaptable to cold)	-30°C to +70°C

Section II highlights the preliminary design considerations involved in the functionality of the sensor. Section III discusses the figure of merit for the performance of the sensor, i.e., the power transmission coefficient (PTC). Subsequently, the impedance matching theory and design procedure for the matching network are discussed in Section IV. Furthermore, in Section V, the selection of the optimal design is made based on the PTC. In Section VI, the physical fabrication and the method for measuring the antenna input impedance are outlined, while Section VII discusses the RFID testing. Finally, in Section VIII, simulation modeling is used to investigate the performance of the proposed sensor in practical settings.

II. PRELIMINARY DESIGN CONSIDERATIONS AND OPERATIONAL OVERVIEW

In this section, we discuss the introductory details and concepts that will assist in understanding the operation of the proposed temperature sensor. We begin by discussing the issues regarding the RFID IC input impedance. Then, we present the frequency shifting theory of the sensor and the selected matching network. Finally, we conclude this section with a discussion on the LCE used in the proposed sensor.

For this sensor design, the Alien Higgs III SOT RFID IC was used. The design of the sensor depends on the input impedance of the RFID IC. Moreover, this input impedance is a function of applied power and frequency of operation [18], [19]. In our design, the input impedance at the minimum power level required for the RFID IC to turn on (i.e., the threshold power) within the RFID operating band of 902–928 MHz is selected. Additionally, this guideline will maximize the read-range capability. The nominal

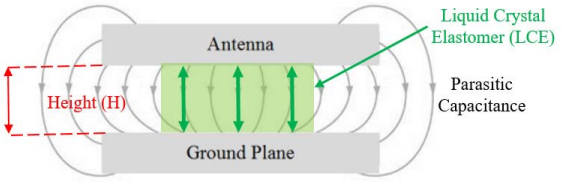

Fig. 1. Operational through the frequency of the sensor is controlled actuation of the designed antenna above the ground plane using LCE technology.

value of $Z_{IC} = 18 - 164j$ was carefully chosen based on [1] and [19].

The frequency self-shifting operation of the proposed sensor is accomplished through the physical design of the sensor. We begin by designing a planar antenna with a customized matching network on an FR4 substrate. This antenna is then placed above a ground plane at a height H, as shown in Fig. 1. The ground plane induces a parasitic capacitance. The relation of the parasitic capacitance to the operating frequency of the developed sensor follows the equation for the resonant frequency of an LC circuit, and is given by [9, p. 136]:

$$f_{res} = \frac{1}{2\pi\sqrt{LC}} \tag{1}$$

where L represents the equivalent inductance of the dipole and C represents the equivalent capacitance plus the induced parasitic capacitance due to the presence of the ground plane [9, p. 254].

Accordingly, the parasitic capacitance is inversely proportional to the height of the antenna above the ground plane analogous to that of a parallel plate capacitor [20]. Also, the parasitic capacitance is inversely proportional to the operating frequency of the sensor. Thus, the height is directly proportional to the operating frequency.

Furthermore, the height between the antenna and the ground plane is controlled by an LCE support which is temperature dependent, refer to Fig. 1. Hence, the operating frequency of the sensor depends on the temperature.

The next design step consists of determining an appropriate matching network to provide a conjugate match between the antenna and the RFID IC for maximum power transfer [21, p. 78]. The T-match and the inductively coupled loop are two common methods for matching RFID antennas [22, pp. 69–71]–[24]. However, the design configurations for these impedance matching methods incorporate feeding loops with permanent physical dimensions. Due to the profound influence of the ground plane, these dimensions would need to be altered as the height, H, changes [25]. Hence, these impedance matching methods impose excessive complexity and are not suitable for our design. For this reason, an innovative integrated T-match network (ITMN) is utilized [26]. The ITMN consists of embedding the classical T-match network (TMN) within the planar dipole antenna structure. Furthermore, the ITMN is a good impedance matching method as it consists of only four design parameters [1], [26]. The heights, H, at which the desired frequency shifts must occur and the detailed design of the matching network are discussed in Section IV.

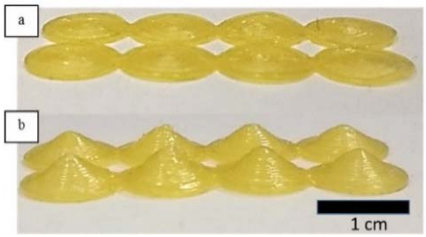

Fig. 2. 4-D-printed LCE 4×2 array with Archimedean chord cells is printed with controlled molecular orientation. (a) The array is depicted in the relaxed state with no heat-stimulus. (b) When a heat-stimulus is applied, each cell forms a conical shape. The total array then provides sufficient lifting force to actuate the antenna.

A. 4-D-Printed Liquid Crystal Elastomers

LCEs are stimuli-responsive polymers [13], [16], [27]. The nematic LCE used here consists of molecules that have orientational order. As heat is applied, the material undergoes a phase transition, and the LCE contracts along the nematic director [13]. As a result, the direction of the thermomechanical response of the LCE is controlled by the orientation of the nematic director [16]. Thus, by controlling the molecular orientation of the LCE, materials that undergo a variety of shape changes can be obtained. In this application, the significant advantage of the LCE, as compared to shape memory polymers is that the material returns to its original state after the heat stimulus has been removed without any physical intervention [16].

A 4-D-printed structure is a 3-D printed structure that is capable of reversibly changing shape due to a stimulus [13]. Here, LCE structures are printed with controlled molecular orientation, refer to Fig. 2(a). The molecular order is programmed by controlling the print path. Therefore, by controlling the print path, 3-D structures with a reversible stimulus response can be fabricated with customized geometries [13]. Furthermore, LCEs printed on nonuniaxial print paths within a plane undergo complex deformation on heating. Specifically, directing the print path along an Archimedean chord pattern results in an LCE film programmed with the nematic director that varies azimuthally around a single point, similar to the director pattern that is observed in a $+1$ topological defect [13]. As a result, this single point is actuated in the direction normal to the resting plane as heat is applied [28]. For application in this paper, to maximize the lifting capacity, a 4×2 array of Archimedean chord cells was fabricated. The array is reversible depending on the applied temperature and is displayed in the relaxed and excited states in Fig. 2(a) and (b), respectively.

III. Power Transmission Coefficient

The Friis transmission equation describes the power received (P_r) by an antenna due to a transmitting antenna at a distance, d, in the far field, and is given by [29, p. 95]

$$P_r = (P_t G_t A_r)/(4\pi d^2) \tag{2}$$

where P_t is the transmitted power, G_t is the gain of the transmitting antenna, and A_r is the effective aperture of

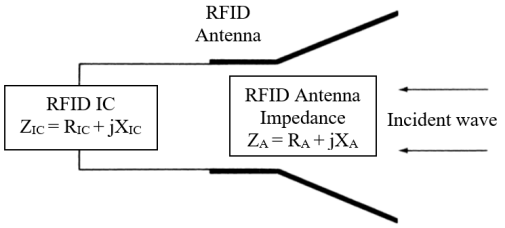

Fig. 3. Schematic of an RFID tag antenna with complex input impedance Z_A terminated to an RFID IC with complex input impedance Z_{IC} in the receiving mode.

the receiving antenna. The schematic of an RFID antenna (in the receiving mode) terminated by an RFID IC is depicted in Fig. 3. The impedances of the RFID antenna and the RFID IC are defined, respectively, as

$$Z_A = R_A + jX_A \tag{3}$$

$$Z_{IC} = R_{IC} + jX_{IC}. \tag{4}$$

Furthermore, the power wave reflection coefficient between the antenna and the IC is expressed as [30], [31]

$$\Gamma = \frac{Z_A - Z_{IC}^*}{Z_A + Z_{IC}}. \tag{5}$$

Consequently, the PTC is then specified as [22, pp. 69–71]

$$\tau = 1 - |\Gamma|^2. \tag{6}$$

Substituting (3)–(5), into (6) brings the PTC to the following form:

$$\tau = \frac{4R_A R_{IC}}{|Z_A + Z_{IC}|^2}. \tag{7}$$

Finally, after combining (2) and (7), an expression for the power received by the IC from a transmitting antenna is written as follows:

$$P_{chip} = (P_t G_t A_r \tau)/(4\pi d^2). \tag{8}$$

Hence, (7) is significant as it describes the degree of matching between the antenna and the IC, where $0 \leq \tau \leq 1$. In the case when $\tau = 1$, a conjugate match ($Z_A = Z_{IC}^*$) is obtained that provides maximum power transfer to the IC [1], [21, p. 78]. It is desirable to design the antenna with a matching network in such a way so as to achieve a transmission power coefficient close to 1. For this reason, τ, as given by (7), is used as a figure of merit for our sensor's performance.

IV. Sensor Design

Commercially available RFID tags employ antennas with matching networks that consist of a variety of customized complex geometries [9, pp. 305–344], [22, pp. 74–80]. In other words, there is no standardized procedure for designing RFID antennas [26]. In contrast, the planar RFID antenna with the ITMN proposed here is advantageous, as it requires only four dimensions to be optimized. Accordingly, these dimensions are L, W, W_1, and s, refer to Fig. 4. Also, in our design, t is set to 1 mm, which provides a favorable distance at the input/output port for the RFID IC pins to make contact.

In this section, using the classical TMN as a basis model, we develop design equations and a procedure to determine the design dimensions: L, W, W_1, and s.

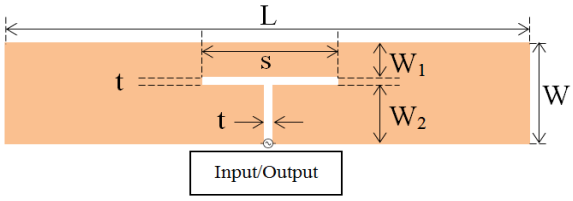

Fig. 4. Planar dipole antenna with the ITMN.

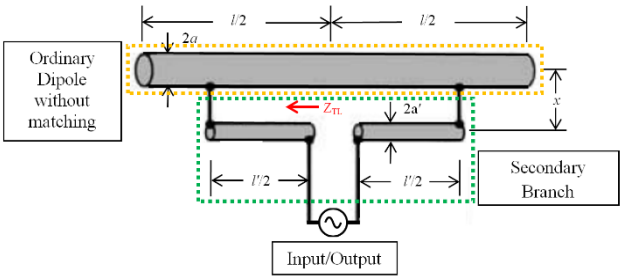

Fig. 5. A secondary branch of conductors is added to an unmatched dipole to achieve an impedance match at the input port by adjusting the dimensions x, l', and a'.

A. Current Division Factor Dependence on Impedances

The TMN is an established impedance matching method for dipole antennas [22, pp. 69–71], [23]. It incorporates a secondary branch of conductors with a small spacing, x, from an ordinary dipole antenna; without any matching network. By adjusting the spacing, x, the length, l', and radius, a', of these conductors, a favorable match can be obtained at the input/output port, refer to Fig. 5 [29, pp. 531–533].

Due to the geometrical asymmetry between the ordinary unmatched dipole and the conductors in the secondary branch, e.g., $a \neq a'$ and $\ell \neq \ell'$, the current at the input is not uniformly divided among the two branches. To account for this nonuniform current distribution, the current division factor, α, based on the geometry is introduced [29, pp. 531–533]

$$\alpha = \frac{\ln\left(\frac{x}{a'}\right)}{\ln\left(\frac{x}{a'}\right) - \ln\left(\frac{a}{a'}\right)}. \tag{9}$$

Furthermore, the TMN in Fig. 5 is conveniently interpreted through the transformer model in Fig. 6. In this case, Z_A is the input impedance of the ordinary dipole antenna without any matching network and Z_{TL} is the shunted transmission line mode impedance, refer to Fig. 5 [26], [29, pp. 531–533]. It is apparent from Fig. 6 that the input impedance is a function of α. Hence, by adjusting the geometry of the secondary branch (i.e., x, l', and a'), α is modified, and one can achieve the desired impedance match at the input port. In our planar dipole antenna design, this impedance matching method will be used.

A formula, introduced in [26], which expresses the current division factor in terms of the planar antenna and RFID IC impedances, is derived and its correlation to the antenna geometry is identified. The input impedance, Z_{IN}, of the TMN from Fig. 6 is written as follows:

$$Z_{IN} = R_{IN} + jX_{IN} = \frac{2Z_{TL}\left[(1+\alpha)^2 Z_A\right]}{2Z_{TL} + (1+\alpha)^2 Z_A}. \tag{10}$$

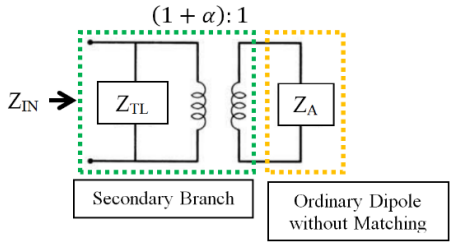

Fig. 6. A Transformer model of the TMN that is depicted in Fig. 5. It is evident that the input impedance is dependent on the current division factor, α. Moreover, α depends on the geometry of the secondary branch.

To achieve maximum power gain, Z_{IN} should be matched to the complex conjugate of the input impedance of the RFID IC [21, p. 78], that is,

$$\mathrm{Z_{IN}} = \mathrm{Z_{IC}^{*}} = \mathrm{R_{IC}} - \mathrm{jX_{IC}}. \tag{11}$$

Moreover, the transmission line mode impedance, Z_{TL}, is essentially a shorted transmission line, refer to Fig. 5 [29, pp. 531–533]. Hence, the impedance Z_{TL} is purely imaginary, or $Z_{TL} = jX_{TL}$. By substituting this transmission line mode impedance and (3) into (10) and setting it equal to (11), the following expression is obtained:

$$\mathrm{Z_{IN}} = \frac{2\mathrm{jX_D}\left[(1+\alpha)^2(\mathrm{R_A}+\mathrm{jX_A})\right]}{2\mathrm{jX_D}+(1+\alpha)^2(\mathrm{R_A}+\mathrm{jX_A})} = \mathrm{R_{IC}} - \mathrm{jX_{IC}}. \tag{12}$$

Furthermore, after equating the real parts and solving for α, the following design equation is obtained:

$$\alpha = -\frac{\mathrm{R_A^2R_{IC}} + \mathrm{R_{IC}X_A^2} - \sqrt{\left(\mathrm{R_AR_{IC}}\left(\mathrm{R_A^2}+\mathrm{X_A^2}\right)\left(\mathrm{R_{IC}^2}+\mathrm{X_{IC}^2}\right)\right)}}{\mathrm{R_{IC}R_A^2} + \mathrm{R_{IC}X_A^2}}$$
$$= \sqrt{\frac{\mathrm{R_A}\left(\mathrm{R_{IC}^2}+\mathrm{X_{IC}^2}\right)}{\mathrm{R_{IC}}\left(\mathrm{R_A^2}+\mathrm{X_A^2}\right)}} - 1. \tag{13}$$

Equation (13) shows that α is a function of the complex impedances of the RFID IC and the planar antenna. Moreover, this equation implicitly shows that α depends on the geometry of the planar antenna. This geometrical relation will be utilized in Section IV-C, to determine the length, L, and width, W, (see Fig. 4) of our planar antenna design using simulation.

B. Current Division Factor Dependence on Geometric Parameters

In this section, we derive the remaining design equation that will determine the width W_1 (see Fig. 4). It should be pointed out that (9) assumes cylindrical conductors are used, as shown in Fig. 5. However, the planar antenna with the ITMN in Fig. 4 is designed using flat planar conductors. To correctly approximate the antenna characteristics using conductors of flat cross section, an equivalent circular conductor must replace the noncircular cross section of the flat planar conductors. This is accomplished by utilizing the electrical equivalent radius (EER) [29, p. 514] as depicted in Fig. 7, where a represents the width of the flat conductor.

Moreover, in Fig. 8, the antenna width, W, consists of three sections of flat conductors. Each conductor is defined using the EER and is labeled as: $\mathrm{EER_{W1}}$, $\mathrm{EER_t}$, and $\mathrm{EER_{W2}}$. The EER

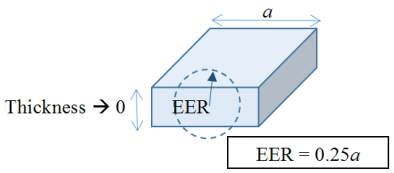

Fig. 7. EER of a flat planar conductor.

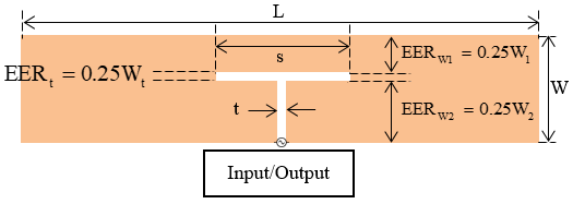

Fig. 8. Planar antenna design with the ITMN and the EERs defined for the flat conductors.

is based on the physical dimensions of the flat conductor as depicted in Fig. 7.

Based on Fig. 5, when calculating the dimension x, the EER of the center spacing in Fig. 8 is doubled, i.e., $2\mathrm{EER_t}$, since the EER represents the equivalent radius and not the diameter. Finally, to adapt (9) to the planar antenna design, the EERs of the flat planar conductors, as shown in Fig. 8, are incorporated into the ratios: x/a' and a/a'. After further simplification, the following expressions are obtained:

$$\frac{\mathrm{x}}{\mathrm{a'}} = \frac{\mathrm{EER_{W1}} + 2\mathrm{EER_t} + \mathrm{EER_{W2}}}{\mathrm{EER_{W2}}} = \frac{\mathrm{W_1} + 2\mathrm{t} + \mathrm{W_2}}{\mathrm{W_2}} \tag{14}$$

$$\frac{\mathrm{a}}{\mathrm{a'}} = \frac{\mathrm{EER_{W1}}}{\mathrm{EER_{W2}}} = \frac{\mathrm{W_1}}{\mathrm{W_2}}. \tag{15}$$

Subsequently, by substituting (14) and (15) into (9), the current division factor for the planar antenna model of Fig. 8 is written as follows:

$$\alpha = \ln\left(\frac{\mathrm{W_1}+2\mathrm{t}+\mathrm{W_2}}{\mathrm{W_2}}\right) \Big/ \left(\ln\left(\frac{\mathrm{W_1}+2\mathrm{t}+\mathrm{W_2}}{\mathrm{W_2}}\right) - \ln\left(\frac{\mathrm{W_1}}{\mathrm{W_2}}\right)\right). \tag{16}$$

Furthermore, the width, W, in Fig. 4 is defined by the equation: $W = W_1 + t + W_2$. Since t is significantly smaller than the dimensions W_1 and W_2, we can use the following expression, with minimal error, for the width, $W = W_1 + 2t + W_2$. This substitution is necessary to format (16) in such a way so as to provide a simplified and concise expression for the upper width, W_1, (refer to Fig. 4). Substituting this approximation in (16) yields the following:

$$\alpha = \ln\left(\frac{\mathrm{W}}{\mathrm{W_2}}\right) \Big/ \left(\ln\left(\frac{\mathrm{W}}{\mathrm{W_2}}\right) - \ln\left(\frac{\mathrm{W_1}}{\mathrm{W_2}}\right)\right). \tag{17}$$

Equation (17) can be solved for W_1

$$\mathrm{W_1} = \left(\mathrm{W}\left(\frac{\mathrm{W_2}}{\mathrm{W}}\right)^{\frac{1}{\alpha}}\right). \tag{18}$$

Moreover, dimension W_2 controls the vertical positioning of the ITMN (see Fig. 4). For a practical design and to further simplify (18) to a function of only one variable, it is assumed

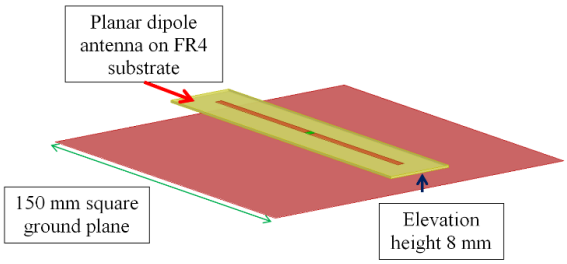

Fig. 9. ANSYS HFSS simulation model of the planar dipole antenna design on an FR4 substrate over the ground plane.

that W_2 is equal to half the width of the antenna, W, i.e., $W_2 = W/2$. Also, we assume that W_1 is an integer to allow for rapid and easy prototyping. Based on these two assumptions, (18) is written as follows:

$$\mathrm{W}_1 = \mathrm{integer}\left(\mathrm{W}\left(\frac{1}{2}\right)^{\frac{1}{\alpha}}\right). \tag{19}$$

Finally, from Fig. 4

$$\mathrm{W}_2 = \mathrm{W} - \mathrm{t} - \mathrm{W}_1 \tag{20}$$

and as mentioned earlier in this section, t is set to 1 mm. Equations (13), (19), and (20) will be used as design equations for the planar dipole antenna with the ITMN. The design process will be detailed in Section IV-C.

C. Design Process

First, an ordinary planar dipole at 928 MHz is designed using an FR4 substrate. The planar antenna is then placed above a 150 mm square ground plane at a height of 8 mm. The FR4 substrate provides a firm support for the RFID IC, which improves the structural integrity of this tag. The design model is shown in Fig. 9.

Then, the width, W, is varied from 10 to 60 mm in intervals of 10 mm. Furthermore, the length, L, is swept from 80 to 180 mm. For each antenna width, W, the antenna input impedance is simulated as the length, L, is swept. Equation (13) is then applied to the simulated input impedances to calculate the current division factor, α, which is depicted in Fig. 10.

Theoretically, any point on a curve in Fig. 10 represents a solution combination of α, W, and L for the planar antenna design depicted in Fig. 4. Accordingly, the combination of α and W at the length (L) of 120 mm reveals design values that are favorable for fabrication. Also, only the three smallest widths of 10, 20, and 30 mm are considered as they provide designs with the smallest weight. The parameters *W, L,* and α are selected from Fig. 10 for the three designs (A, B, and C) and are listed in Table II.

Subsequently, (19) and (20) are now utilized to find the widths W_1 and W_2, respectively, for each of the selected designs. The widths W_1 and W_2 are shown in Table II.

At this point, all the design dimensions have been determined except for the length, *s*. To determine this length, each design in Table II is modeled (in simulation) individually as shown in Fig. 11. Furthermore, each design is placed 8 mm above the ground plane. Finally, the length, s, is then swept until the operating frequency of the antenna is 930 MHz. Table II summarizes these results.

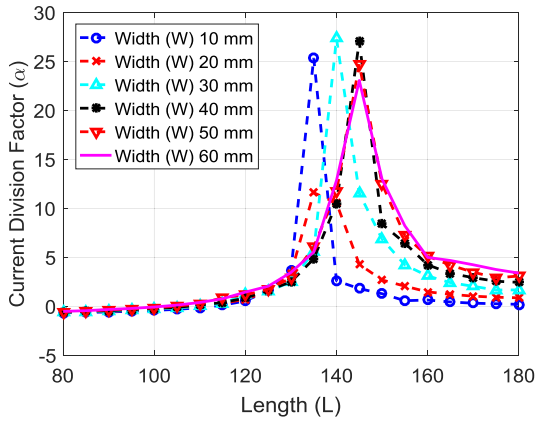

Fig. 10. Current division factor, α, for different dipole lengths and widths.

TABLE II
FINAL DESIGN DIMENSIONS WITH THE HEIGHTS THAT CORRESPOND TO OPERATING FREQUENCIES

Design	W (mm)	L (mm)	α	W_1 (mm)	W_2 (mm)	s (mm)	Heights 902MHz 928MHz
A	10	120	0.55	2	7	9.8	3.6mm 7.2mm
B	20	120	0.74	7	12	9.4	3.6mm 6.8mm
C	30	120	1.23	17	12	17.7	2.8mm 6.8mm

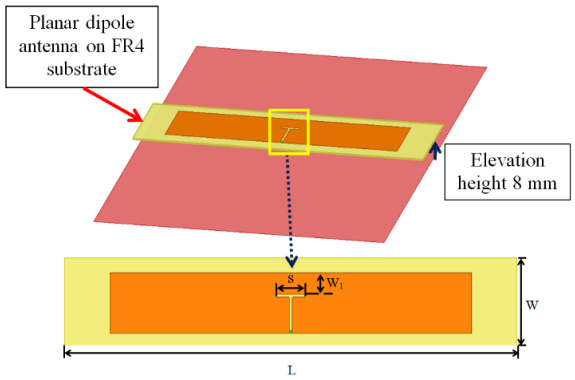

Fig. 11. ANSYS HFSS simulation model of the planar antenna design with the ITMN.

Section II showed that when the planar antenna decreases its height from the ground plane, its operating frequency decreases as well. Therefore, operating at 930 MHz at a height of 8 mm serves as a starting point. Accordingly, the antenna is then lowered incrementally to find the correct operating heights that correspond to the operating frequencies of 902 and 928 MHz, refer to Table II.

It is important to recollect that this sensor conveys temperature threshold crossings in the frequency domain. For that reason, the sensor is designed to have the largest change in

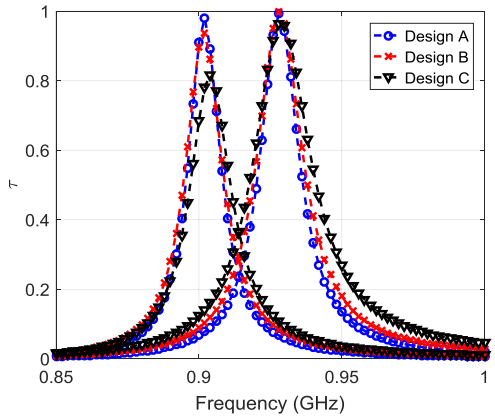

Fig. 12. PTC versus frequency for designs A, B, and C, from Table II. This plot depicts the performance of each design at the two operating frequencies of 902 and 928 MHz.

operating frequencies so as to make it easily discernable to the operator that a temperature threshold has been crossed. Hence, the lowest and the highest possible design frequencies within the RFID UHF band are utilized, that is, 902 and 928 MHz, respectively.

In this section, we have discussed the process of finding the correct dimensions of the planar antenna with the ITMN. Equations (13), (19), and (20) were used to find the L, W, W_1, and W_2 of the design, respectively. Finally, simulation optimization was used to find the length, *s,* and the operating heights.

V. Optimum Design Selection

The purpose of this section is to select the optimal design from Table II for fabrication. The level of performance of each design is determined using the PTC, τ, as discussed in Section III. The PTC is plotted for each design using (7) in Fig. 12. It is apparent that the PTC is maximum at the two intended operating frequencies of 902 and 928 MHz which correspond to the lower and higher elevation heights above the ground plane, respectively. Finally, it can be concluded that designs A and B exhibit better performance than design C as their PTC is larger at the two operating frequencies.

Designs A and B are comparable in terms of their PTC performance. In contrast, these two designs differ in the heights required to operate at 928 MHz. That is, from Table II, Design A requires an actuation of 3.6 mm (7.2–3.6 mm) and Design B requires an actuation of 3.2 mm (6.8–3.6 mm). This means that Design B requires a smaller amount of actuation to transition between the two operating frequencies of 902 and 928 MHz. Thus, the smaller height difference of design B requires the application of a less heat stimulus, which extends the life of the LCE actuator by avoiding overheating and/or overstretching. For this reason, Design B is selected for fabrication in this paper.

A. Sensor Radiation Performance

In this section, we examine the radiation performance of the designed sensor. The radiation pattern and the gain of the developed sensor are similar for the two cases where the designed antenna is 3.6 mm (operating at 902 MHz) above the ground plane and where the designed antenna is 6.8 mm (operating at 928 MHz) above the ground. The radiation pattern resembles that of a basic dipole; however, the radiation is directed towards the antenna side (due to the presence of the ground plane behaving as a reflector) where the maximum gain is 3.7 dBi in both cases. The 3-D radiation pattern is shown in Fig. 13.

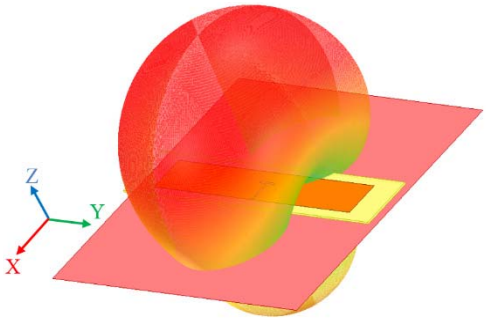

Fig. 13. HFSS modeling of the 3-D radiation pattern of the designed sensor. The radiation pattern and the maximum gain are similar for both cases when the antenna is elevated above the ground plane to 3.6 mm (operating at 902 MHz) and when antenna is elevated to 6.8 mm above the ground plane (operating at 928 MHz).

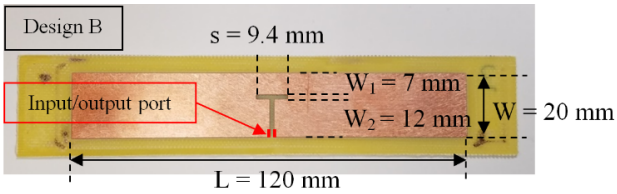

Fig. 14. Prototype of the planar antenna design with ITMN.

VI. Sensor Prototyping and Performance Testing

Design B was fabricated using an LPKF S103 micromilling machine. The prototype is depicted in Fig. 14. The impedance of this antenna needs to be measured without the IC to validate our simulation results and the design methodology. This measurement is accomplished by using a customized differential probe or test fixture in a procedure that will be discussed in what follows.

A. Impedance Measurement

A coaxial cable is a convenient type of transmission line that is commonly used to take RF measurements. However, due to its asymmetry (i.e., having nonidentical inner and outer conductors), a coaxial cable is an unbalanced transmission line. Therefore, when a coax is connected to a balanced antenna, such as a dipole, a net-current flows to the ground on the outer surface of the outer conductor [29, pp. 539–541], [32]. Thus, the input impedance of our dipole, Fig. 14, cannot be measured through a standard measurement of the S_{11}.

As discussed in [33] and [34], the solution is to bisect the input/output port, refer to Fig. 14, into two individual ports with reference to a newly introduced common ground. The impedance is then derived based on the differential voltage between the two ports of the network and is correlated to

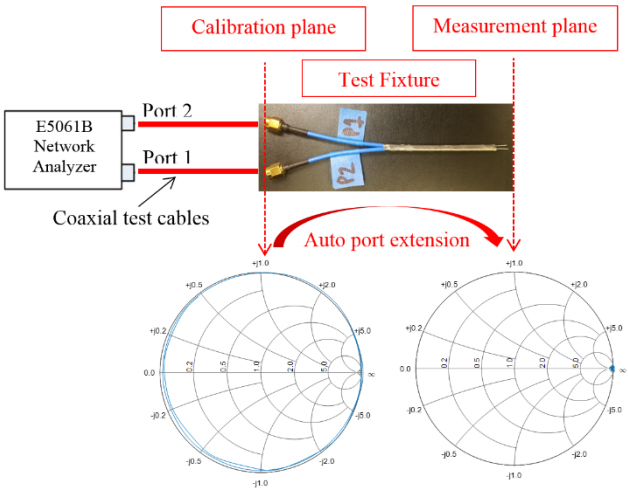

Fig. 15. Fabricated input impedance test fixture and calibration process.

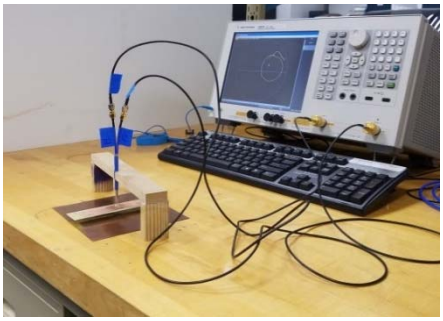

Fig. 16. Impedance measurement setup with test fixture and VNA.

the equivalent two-port scattering parameters. To introduce a common ground and perform the full two-port measurement, a customized test fixture is fabricated.

The test fixture is fabricated by shorting the outer conductors of two coaxial cables and leaving the inner conductors untouched in an open circuit formation. The shorted outer conductors serve as the common ground between the two inner conductors of the cables. Furthermore, the Keysight E5061B vector analyzer is used to perform the measurements. A standardized calibration kit is used to align the reference plane from the ports of the VNA to the end of the coaxial test cables. However, this calibration process cannot electrically account for the test fixture. To resolve this, E5061B offers an Auto Port Extension capability to account for the electrical length of the test fixture [35].

The test fixture and the calibration process are shown in Fig. 15. Once the VNA is calibrated, the test fixture is attached and the response is depicted in the left Smith chart in Fig. 15. Once the VNA runs the auto port extension of the open-circuited test fixture, the corresponding open-circuited response in the right Smith chart in Fig. 15 is obtained. After completing this step, the instrumentation is fully calibrated and the effects of our text fixture have been corrected. Subsequently, the planar dipole antenna of Fig. 14 is soldered at the "input/output" port to the inner conductors of the test fixture. The full two-port S-parameters are then taken at the two heights corresponding to the two operating frequencies

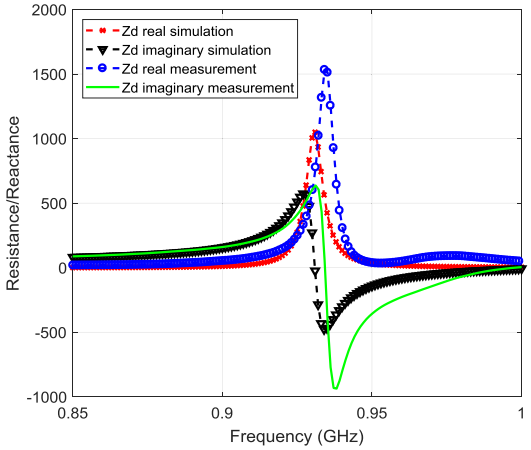

Fig. 17. Simulated and measured complex input impedances when the elevation of the planar dipole is 3.6 mm above the ground plane. This elevation corresponds to the operating frequency of 902 MHz.

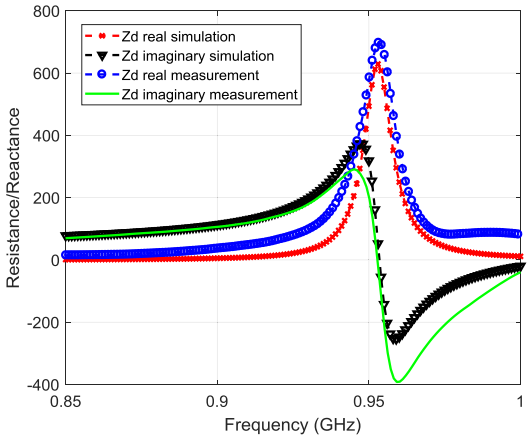

Fig. 18. Simulated and measured complex input impedances for when the elevation of the planar dipole is 6.8 mm above the ground plane. This elevation corresponds to the operating frequency of 928 MHz.

902 and 928 MHz of Design B in Table II. The test setup is depicted in Fig. 16.

Once the data are collected, the complex input impedance of the balanced antenna is determined from the measured scattering parameters as follows [33]:

$$Z_{in} = \frac{2Z_0(1 - S_{11}S_{22} + S_{12}S_{21} - S_{12} - S_{21})}{(1 - S_{11})(1 - S_{22}) - S_{21}S_{12}}. \quad (21)$$

Finally, the measured and simulated complex input impedances are compared in Figs. 17 and 18 for the heights of 3.6 and 6.8 mm which correspond to the operating frequencies of 902 and 928 MHz, respectively. Our simulated and measured data agree well. The small discrepancy between them occurs because of the parasitic fields induced by the metallic test fixture near the ground plane, which is not included in the simulation [22, pp. 84–86], [9, pp. 340–342].

Also, the PTCs, using (7), for both the simulated and measured impedance data, are compared in Fig. 19. In other words, this plot shows a comparison of the measured and simulated power that is delivered to the RFID IC. Both measurements and simulations show that maximum power is delivered to the RFID IC very close to the intended frequencies

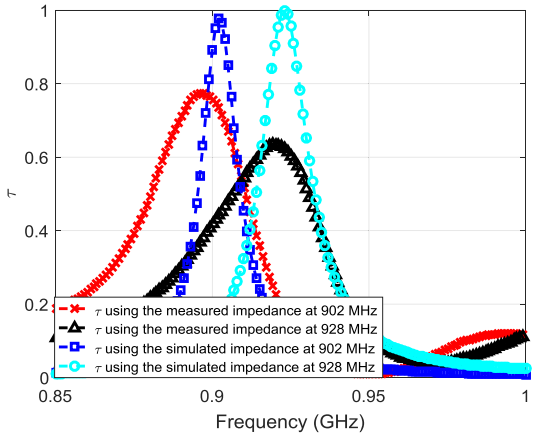

Fig. 19. PTC using the simulated and measured antenna input impedances.

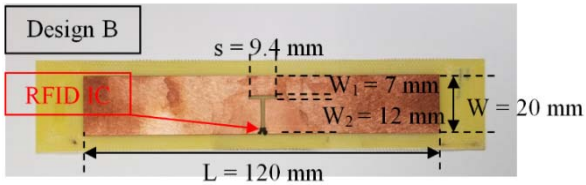

Fig. 20. Prototype of the passive RFID tag.

of 902 and 928 MHz, which correspond to the two elevation heights of 3.6 and 6.8 mm, respectively.

VII. Passive Temperature Sensor

In this section, the final design of the RFID sensor is fabricated and tested using the ThingMagic Pro RFID reader. The passive sensing tag is constructed by bonding the RFID IC to the antenna of Fig. 14 using electrically conductive glue. The prototyped tag is shown in Fig. 20.

The developed sensor has a low overall material and fabrication cost. Also, the materials required to fabricate the antenna for the developed sensor include readily available materials, that is, a single-sided FR4 board, a copper metal ground plane, and a plastic spacer. Moreover, the fabrication process for the high-temperature reactive 4-D-printed LCE array is optimized and easily repeatable. The materials required for preparing the liquid crystal ink used in the printing process of the 4-D LCE array are inexpensive and easily accessible as commercial products [13]. The total processing time is less than one day with the most time-consuming process being the oligomerization of the materials which may take up to 12 h [13]. Once the liquid crystal ink is prepared, the printing of the actual LCE structure is conducted in approximately one hour using custom CAD files for the desired LCE structure. Overall, the fabrication process of the 4-D-printed LCE array is simple and cost-effective.

A. RFID Measurement Setup

A schematic of our RFID measurement setup is depicted in Fig. 21. The reader emits an electromagnetic continuous wave (CW) signal towards the sensor. In return, the sensor and the surrounding environment reflect or backscatter the CW signal. The returned response of the sensor is modulated to

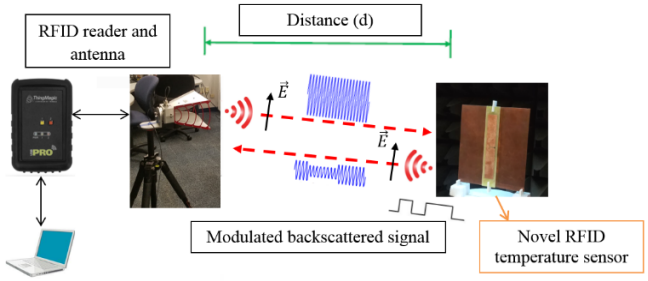

Fig. 21. RFID measurement setup with the vertical polarization orientation.

differentiate the response of the sensor from the background environment [9, pp. 70–77], [36]. In our setup, the developed sensor utilizes a linearly polarized dipole antenna and the reader is connected to a linearly polarized double-ridged horn antenna with a gain of 7 dBi [37]. During all measurements, the developed sensor and horn antenna were oriented with vertical polarization (perpendicular to the ground) as depicted in Fig. 21.

When both the reader and the tag are vertically polarized with respect to the ground plane and have a common E-plane, the readability of the sensor is optimal. In the worst case, when the planes become orthogonal, the link between the reader and the sensor is maximally deteriorated [9, p. 330]. This polarization alignment issue is independent of the operational physics of the sensor. Hence, a change in the orientation between the reader and the single sensor can only affect the ability to read the sensor with a negligible impact on the temperature detection accuracy of the developed sensor. Additionally, in situations where the tag orientation is ambiguous, such as a shipping loading dock, circularly polarized reader antennas are deployed. This way, a linearly polarized tag can be readily read with any orientation considering a 3 dB power loss due to the circular-to-linear polarization mismatch [9, p. 270]. Furthermore, the issue on the temperature detection accuracy of the developed sensor when dual sensors are in close proximity with various orientations between them is addressed in Section VIII.

Since the sensor designed in this paper shifts operating frequencies to convey changes in temperature, it is critical to measure the operating frequency of the sensor. To obtain this measurement, the power of the RFID reader is increased in increments of 0.1 dBm until the threshold power of the RFID IC is reached. The threshold power is identified as the minimum power level at which data begin to be retrieved from the temperature sensor [9, pp. 70–77], [18], [36]. This transmitted power at which the developed sensor responds is the measurement recorded and is conducted for every frequency in increments of 1 MHz in the 902 to 928 MHz band. The frequency at which the least transmitted power is required to receive data from the tag is therefore its operating frequency. Finally, this procedure is repeated to verify that the data collected are consistent, and therefore reliable.

Furthermore, there are two RFID measurement setups that were used to demonstrate the functionality of the novel RFID temperature sensor. Initially, a static setup was used to prove the operation of the sensor. Then, a dynamic setup was used

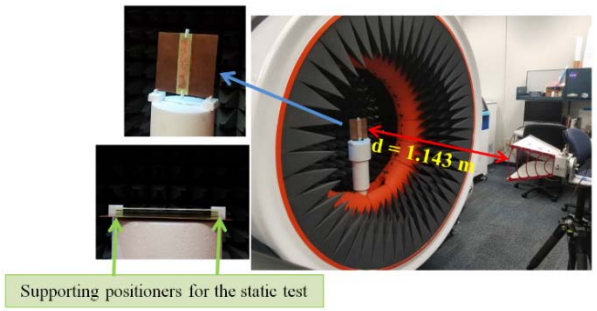

Fig. 22. Static test setup of the proposed RFID tag.

to demonstrate the operation of the sensor in a temperature varying environment.

B. Static Testing

This setup demonstrates the frequency shifting capability of the sensor as the height of the planar antenna changes above the ground plane. The 3-D printed supporting positioners were fabricated to place the designed antenna (i.e., Design B) at the calculated heights above the ground plane, as shown in Table II. This test setup is depicted in Fig. 22, where the distance between the sensor and the reader antenna is 1.143 m.

It should be noted that the 3-D printed supporting positioners were not included in the simulation. As per our simulation results, the heights of 3.6 and 6.8 mm provide operating frequencies, for the developed sensor, of 902 and 928 MHz, respectively. Our measurements showed that for the height of 3.6 mm, the measured operating frequency was slightly higher. This is attributed to the presence of positioners. As a result, the height of 3.6 mm, which had been obtained through simulation, had to be slightly adjusted to 3.1 mm during our measurements for the tag to operate at 902 MHz with the supporting positioners present. The adjustment was made by incrementally trimming the positioners and the final height of the positioner was found using electronic precision calipers. In contrast, the height of 6.8 mm in our measurements provided the desired operating frequency of 928 MHz and no adjustment was needed. According to [9, pp. 340–342] and [38], the relation of the capacitance to the gap separation is asymptotic. Specifically, as the gap increases, the effect on the capacitance reduces. Thus, it is justifiable that for the lower height a slight adjustment is needed (from 3.6 to 3.1 mm), since the effect of the supporting positioners on the capacitance is more significant for the lower height than for the larger height (6.8 mm).

Our static measurements for the two heights of 3.1 and 6.8 mm are depicted in Fig. 23. For the height of 3.1 mm, the transmitted power is minimum at 902 MHz which corresponds to the tag's operating frequency. As the height is increased to 6.8 mm, the operating frequency transitions to 928 MHz, where the transmitted power is the least. As detailed in Section II, the trend observed in Fig. 23 obeys (1) and the fact that the parasitic capacitance between the antenna and the ground plane is inversely proportional to the height, H (see Fig. 1), which is known from parallel-plate capacitor theory [20]. Specifically, as the height decreases the parasitic capacitance increases and according to (1) the resonant frequency decreases. Moreover, as the height increases the parasitic capacitance decreases and according to (1) the resonant frequency increases. Therefore, the results obtained in Fig. 23 follow the theory correctly and prove that the tag operates as intended, i.e., when the antenna is set to the heights of 3.1 and 6.8 mm above the ground plane, the sensor operates at 902 and 928 MHz, respectively. This logic also supports the results obtained during the dynamic test conducted in Section VII-C.

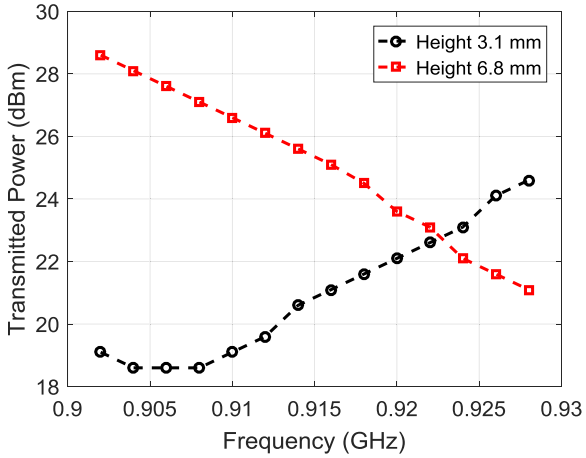

Fig. 23. Static measurements of the RFID tag at two different heights.

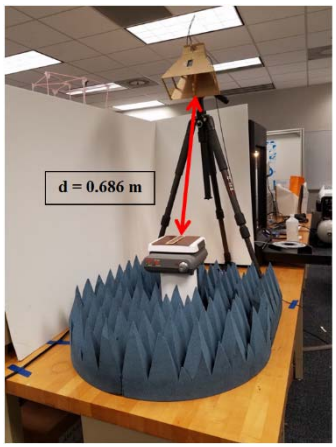

Fig. 24. Dynamic test setup of the proposed passive RFID temperature sensor.

C. Dynamic Testing

In this section, dynamic testing of our RFID sensor will be performed to verify its operation at different temperatures. The 4-D-printed LCE Archimedean chord array was placed between the antenna and the ground plane, refer to Figs. 1 and 2. Furthermore, the sensor was then placed on a hot plate that served as the heat source. This test setup is shown in Fig. 24, where the distance between the sensor and the reader antenna was 0.686 m.

Using electronic precision calipers, the LCE array in its relaxed flat state was measured to have a thickness of 1.045 mm. Accordingly, a 3-D printed spacer with a thickness of 2.055 mm was placed between the antenna and the LCE array to support the antenna at the required height

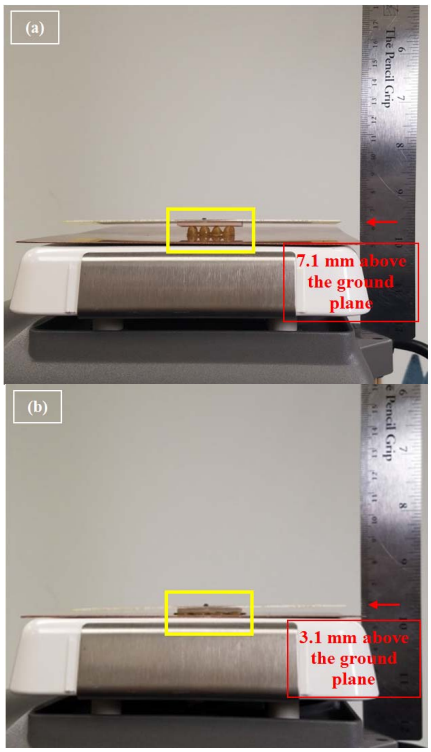

Fig. 25. Dynamic RFID test setup with the heat source that is used to stimulate the LCE array. (a) As the heat source is activated, the LCE raises the RFID antenna by 4 mm at 160 °C. (b) As the heat source is turned off and returns to room temperature, the LCE returns to its original flat state.

of 3.1 mm above the ground plane. As the temperature increases, the flat 4-D-printed LCE array expands into a conical shape in the direction normal to the ground plane, thereby increasing the height of the antenna above the ground plane. The maximum actuation displacement of the LCE array was measured to be 4 mm using a measuring ruler (see Fig. 25). Specifically, when the temperature of the LCE array reaches 160 °C, the LCE array raises the antenna by 4 mm to reach a height of 7.1 mm above the ground plane (which is very close to 6.8 mm as determined by simulation).

The measurements of our dynamic test are shown in Fig. 26. The data confirm that our RFID passive sensor operates as expected. Specifically, at room temperature, the LCE is in its flat and relaxed state holding the antenna 3.1 mm above the ground plane. At this height, the measured transmitted power is minimum at 902 MHz, which corresponds to the intended operating frequency; this is conveyed by the black trace in Fig. 26. Moreover, as the heat source is activated, the LCE actuates the antenna to 7.1 mm above the ground plane, refer to Fig. 25. Consequently, the measured transmitted power is minimum at 928 MHz, which corresponds to the intended operating frequency; this is depicted by the red trace in Fig. 26. Furthermore, to justify the repeatable nature of the developed sensor, when the LCE array returned to room temperature a second test was conducted as shown by the cyan trace where the operating frequency has returned to 902 MHz. Subsequently, the heat stimulus was applied once again to the LCE array and the operating frequency shifted as intended to 928 MHz, which is depicted by the blue trace

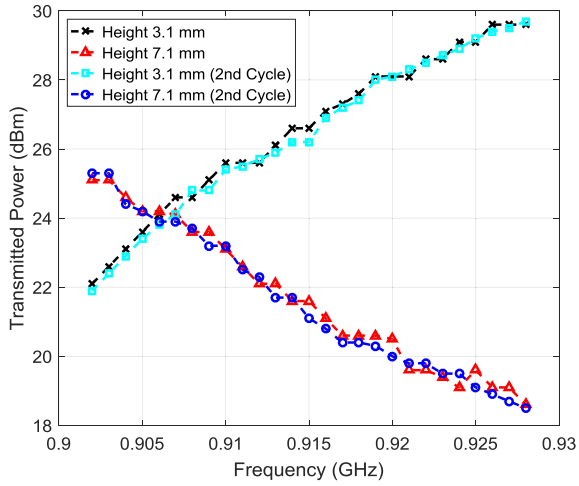

Fig. 26. Dynamic measurements of the RFID tag at two different heights.

in Fig. 26. The performance of the second test matches that of the initial test. Hence, this proves the capability of the developed sensor to measure temperature threshold violations multiple times. In this design, after running multiple hot and cold temperature cycles, it was observed that the 4-D-printed 4×2 LCE Archimedean chord array takes an average of 25 s to return to its relaxed-flat state after the heat stimulus has been removed.

In addition, due to the actuation of the designed antenna above the ground plane, the transition of the operating frequencies between 902 and 928 MHz for the developed sensor is continuous. Therefore, a linear approximate expression relating the detected temperature to the frequency of operation of the developed RFID temperature sensor can be formulated as follows:

$$\text{Temperature} = 5.296 \times (\text{Frequency}) - 4730. \tag{22}$$

This formulation is appropriate within the frequency boundary of 902–928 MHz, and the temperature and frequency are in degrees Celsius and MHz, respectively.

Moreover, our measurements validate our simulation results and design methodology. To our knowledge, this temperature sensor is unique because of the following.

1) It is passive, i.e., no battery is needed, thereby having very long lifetime and very low cost.
2) It can be reused multiple times (vs. other current sensors that can only detect one temperature threshold [39]) to monitor when the temperature reaches a high-temperature threshold as well as when the temperature drops below the temperature threshold.
3) It provides continuous monitoring of goods that assists in the intelligent assessment of their quality.

Finally, the RFID IC used in this paper was the Alien Higgs III. The temperature of 160 °C where the developed sensor operates at far exceeds the operating temperature range where the input impedance of the RFID IC remains constant, which is from −50 °C to 85 °C [18]. However, this elevated temperature has a negligible impact on the RFID IC input impedance since the RFID IC is partially isolated from the

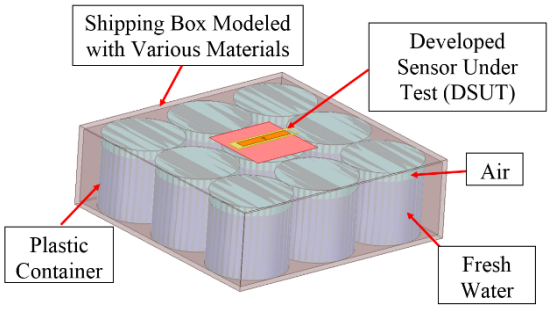

Fig. 27. Simulation model of the shipping box modeled with various materials properties and with a payload of fresh water representing fruits and vegetables.

heated ground plane. That is, the designed antenna with the integrated matching network (ITMN) is supported above the ground plane by the LCE array and spacer, refer to Fig. 25.

As a result, the designed antenna which supports the RFID IC never reaches the temperature of the ground plane (160 °C). During experimentation, using an inferred thermometer, the temperature at the RFID IC was observed to reach approximately 65 °C. This measured temperature is well within the manufacturer's range of operating temperatures, where the input impedance of the RFID IC remains constant; hence, the input impedance of the RFID IC is unaffected. In contrast, if the entire sensor developed in this manuscript is exposed to a temperature of 160 °C, the sensor is not expected to function adequately as the temperature has greatly exceeded the RFID IC manufacturer's specifications. However, the design presented in this manuscript is a proof-of-concept (envisioned to reversibly detect changes in the ambient temperature of the cold-supply chain using LCE technology) which can be readily retrofitted to operate at lower temperatures using cold-reactive LCEs which are currently under development by our team.

VIII. Simulation Modeling for Practical Applications

In this section, we use simulation modeling to test the performance of the developed sensor in practical settings. That is, we first test the performance of the developed sensor when placed on shipping boxes made of various materials carrying a payload that represents fruits and vegetables. Subsequently, we test the temperature detection accuracy of the developed sensor by placing an identical sensor in close proximity at different orientations. In this case, both sensors are placed on individual shipping boxes that are modeled as cardboard with payloads that represent fruits and vegetables. ANSYS HFSS was used for our simulation modeling.

A. Testing on Shipping Boxes Made of Various Materials

Fruits and vegetables are a common perishable payload in the cold-supply-chain and consist mostly of water [40]. Thus, we model a batch of nine plastic bottles filled with fresh water fitted into a shipping box. Moreover, the typical materials used for containing such perishable items during delivery in the cold-supply chain vary and consist of cardboard, wood, and plastic [41]. For that reason, in our simulation test, we keep the payload (plastic bottles with fresh water) constant and vary the material properties of the shipping box. A 508 x 508 x 165 mm3 box with 3 mm thickness is constructed and the relative permittivity and loss tangent are appropriately set to represent the material properties of cardboard, wood, and plastic [42], [43]. Subsequently, the box was modeled as a perfect electric conductor (PEC) to study the effect of mounting the proposed sensor on large metallic structures. In each case, the developed sensor was placed on the box and actuated at the predetermined heights where the sensor operates at 902 and 928 MHz when no box and/or payload is present. The simulation model is shown in Fig. 27.

The results of varying the materials properties of the shipping box are depicted in Fig. 28. The results depict the PTC when the DSUT is at room-temperature operating at 902 MHz; also, when the DSUT has reached the temperature threshold and operating at 928 MHz. The magenta and brown traces are provided as a performance reference and represent the frequency response of the DSUT when no shipping box is present at 902 and 928 MHz, respectively. The remaining traces represent the frequency response of the DSUT at room temperature (where the DSUT operates at the lower end of the RFID band) and at elevated temperatures (where the DSUT operates at the higher end of the RFID band) when mounted on top of the shipping box for different materials properties of the box (cardboard, wood, plastic, and metal).

In general, the presence of the shipping box increases the parasitic capacitance. Based on the results shown in Fig. 28, when the shipping box is present, the two operating frequencies (i.e., one at the lower end and one at the higher end of RFID band) of our proposed antenna decrease compared to when no box is present, i.e., reference curves. Also, when the shipping box is present, the PTC decreases due to the losses associated with the various materials used to simulate the shipping box and the goods [39], [40]. Although there is a shift in the operating frequency along with a decrease in the PTC, the performance of the developed sensor under test (DSUT) remains promising. Specifically, considering the lower limit of the RFID UHF band (near 902 MHz), the shifts of the lower frequency response for all the different shipping boxes are minor (the greatest shift is for the metal shipping box that reduces the operating frequency of our sensor to 899 MHz). Moreover, at 902 MHz (the start of the RFID UHF band), the PTC is approximately 80% for all the different shipping boxes compared to 95% for the case with no shipping box. Considering the upper limit of the RFID UHF (near 928 MHz), the largest frequency shift occurs again for the metal shipping box when the maximum PTC is 97% at 923 MHz. Additionally, the upper frequency responses for all the other shipping boxes have a maximum PTC larger than 85% at approximately 925 MHz. In summary, the above simulation results indicate that the developed sensor can still successfully detect temperature threshold crossings with good separation in the RFID UHF band even in the presence of perishable goods packaged in shipping boxes of various materials.

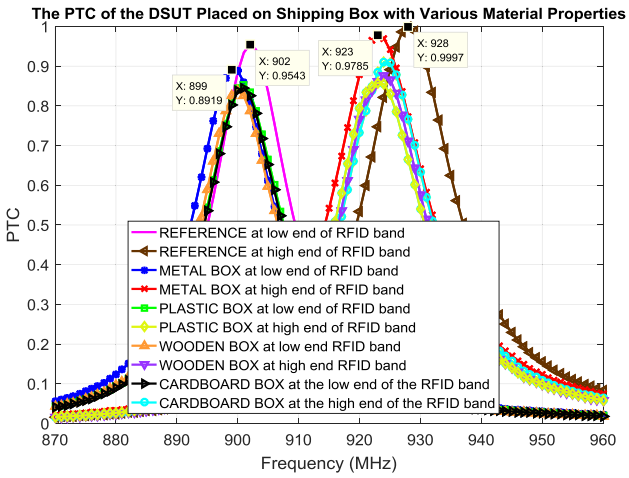

Fig. 28. PTC simulation results of the developed sensor when placed on a shipping box made of different materials properties.

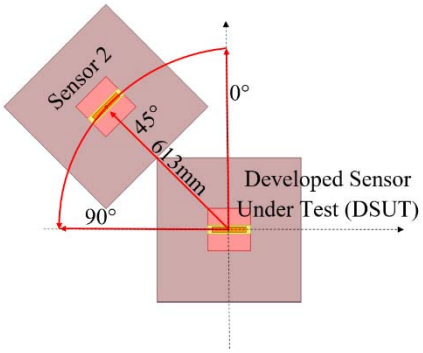

Fig. 29. ANSYS HFSS simulation model with multiple sensors to test the susceptibility in the temperature detection accuracy of the DSUT.

B. Testing With Dual Sensors With Varying Orientation

In this section, we develop a simulation model to study the temperature detection accuracy of the DSUT in the presence of additional sensors on practical items with varying orientations. The developed model of the cardboard shipping box is used with the payload that represents fruits and vegetables. The DSUT is placed on the top of such a box, as shown in Fig. 27 and detailed in the previous section. Subsequently, a pair of these models is placed adjacent to each other. The first sensor (DSUT) along with the corresponding shipping box is placed at the origin and the second sensor along with its corresponding box is rotated at 0°, 45°, or 90° around the DSUT. The setup of this simulation test is shown below in Fig. 29.

For each position of the second sensor and corresponding shipping box (i.e., 0°, 45°, and 90° in Fig. 29), the DSUT is tested in the relaxed and excited states with the second sensor in the relaxed state. Second, the same test is repeated; however, the second sensor is in the excited state. The results of our simulations indicate that when the DSUT is operating in the relaxed state, the performance is unaffected by the presence of the second sensor with its shipping box in this setup. Specifically, this performance is irrespective of the orientation and state of the second sensor. Also, the DSUT always operates sufficiently with a PTC of above 80% at 902 MHz (which is the starting frequency of the RFID UHF band).

Moreover, when the DSUT is excited in the presence of the second sensor, its operating frequency shifts to 915 MHz (923 MHz was the operating frequency of the single excited DSUT on a shipping box). Also, regardless of the state or orientation of the second sensor (and its corresponding shipping box), the DSUT always operates at 915 MHz in the presence of the second sensor in this setup. Also, the DSUT always operates sufficiently with a PTC of above 85% at 915 MHz.

Finally, this simulation test conveys that the temperature detection capability of the developed sensor is unaffected by the presence of the second sensor and the corresponding shipping box. That is, at room temperature the sensor will be read at 902 MHz (as this is the starting frequency of the UHF RFID band) and when the temperature reaches a certain threshold it will be read at 915 MHz. These two frequencies are 13 MHz apart, which provides sufficient separation to detect that a temperature threshold has been reached.

IX. Conclusion

In this research, a novel passive (i.e., battery-free) RFID temperature sensor is developed, analyzed, and validated. The sensor consists of a planar dipole antenna that is actuated above a ground plane. Consequently, the actuation causes the frequency shift. A unique 4D-printed LCE array provides the temperature dependent actuation of the antenna above the ground plane that is reversible and repeatable. Additionally, the planar dipole antenna is customized with the ITMN to match the antenna to the RFID IC at both 902 and 928 MHz operating frequencies.

Furthermore, the antenna was fabricated and the input impedance was measured using a customized differential test fixture. The final design was then verified with two test setups using a commercially available RFID reader. All measured data met favorably with the theory and simulation. The sensor is novel and practical as it self-tunes its operating frequency as temperature changes in a continuous fashion. This is done without any physical intervention. Finally, the cost effectiveness and longevity of the sensor is ensured since the device is fully passive.

Our sensor design can be retrofitted with the appropriate LCEs to detect different ranges of temperature change. Also, the unique advantage of LCEs compared to other active materials is their ability to operate reversibly and they are reusable as they can go through many high/low temperature actuation cycles. Finally, 4-D printed LCE structures that operate at cold temperatures are currently under development by our team.

References

[1] R. Bhattacharyya, C. Floerkemeier, S. Sarma, and D. Deavours, "RFID tag antenna based temperature sensing in the frequency domain," in *Proc. IEEE Int. Conf. RFID*, Orlando, FL, USA, Apr. 2011, pp. 70–77.

[2] P. Kumar, H. W. Reinitz, J. Simunovic, K. P. Sandeep, and P. D. Franzon, "Overview of RFID technology and its applications in the food industry," *J. Food Sci.*, vol. 74, no. 8, pp. R101–R106, Oct. 2009.

[3] K. B. Biji, C. Ravishankar, C. N. Mohan, and T. S. Gopal, "Smart packaging systems for food applications: A review," *J. Food Sci. Technol.*, vol. 52, no. 10, pp. 6125–6135, Oct. 2018.
[4] Ams.usda.gov. (2008). *Protecting Perishable Foods During Transport by Truck*. Accessed: May 5, 2018. [Online]. Available: https://www.ams.usda.gov/sites/default/files/media/TransportPerishableFoodsbyTruck%5B1%5D.pdf
[5] Temptrust.mesalabs.com. (2001). *Recommendations on the Control and Monitoring of Storage and Transportation Temperatures of Medicinal Products*. Accessed: May 5, 2018. [Online]. Available: https://temptrust.mesalabs.com/wp content/uploads/sites/47/2012/05/MHRAcon007569.pdf
[6] A. Dada and F. Thiesse. (2018). *Sensor Applications in the Supply Chain: The Example of Quality-Based Issuing of Perishables*. Accessed: May 14, 2018. [Online]. Available: https://rd.springer.com/content/pdf/10.1007%2F978-3-540-78731-0_9.pdf
[7] United World Transportation. (2018). *The 4 Most Common Cold Chain Logistics Problems Truckers Face and Tips for Solving Them*. Accessed: May 6, 2018. [Online]. Available: https://unitedworldtransportation.com/4-common-cold-chain-logistics-problems-truckers-face-tips-solving/
[8] U. Facts. (2018). *Topic: Organic Food Industry*. Accessed: May 14, 2018. [Online]. Available: www.statista.com and https://www.statista.com/topics/1047/organic-food-industry/
[9] D. Dobkin, *The RF in RFID*, 1st ed. Amsterdam, The Netherlands: Elsevier, 2008.
[10] Infratab Inc. (2018). *Freshtime Tags*. Accessed: Jul. 7, 2018. [Online]. Available: http://infratab.com/freshtime-tags/
[11] Identec Solutions. (2018). *Automated Reefer Container Monitoring—Identec Solutions*. Accessed: Jul. 7, 2018. [Online]. Available: https://www.identecsolutions.com/ports-terminal-industry-solutions/reefer-monitoring/
[12] (2018). *Rfidjournal.net*. Accessed: Jul. 7, 2018. [Online]. Available: http://www.rfidjournal.net/masterPresentations/live2009/np/Finalist_IDS_Microship.pdf
[13] C. P. Ambulo, J. J. Burroughs, J. M. Boothby, H. Kim, M. R. Shankar, and T. H. Ware, "Four-dimensional printing of liquid crystal elastomers," *ACS Appl. Mater. Inter.*, vol. 9, no. 42, pp. 37332–37339, Nov. 2017.
[14] J. Küpfer and H. Finkelmann. (1991). *Nematic Liquid Single Crystal Elastomers*. Accessed: Aug. 24, 2018. [Online]. Available: https://onlinelibrary.wiley.com/doi/pdf/10.1002/marc.1991.030121211
[15] R. S. Kularatne, H. Kim, J. M. Boothby, and T. H. Ware, "Liquid crystal elastomer actuators: Synthesis, alignment, and applications," *J. Polym. Sci. B, Polym. Phys.*, vol. 55, no. 5, pp. 395–411, Mar. 2017. Accessed: Aug. 24, 2018. doi: 10.1002/polb.24287.
[16] J. S. Gibson, X. Liu, S. V. Georgakopoulos, J. J. Wie, T. H. Ware, and T. J. White, "Reconfigurable antennas based on self-morphing liquid crystalline elastomers," *IEEE Access*, vol. 4, pp. 2340–2348, 2016.
[17] C. Liu, H. Qin, and P. T. Mather, "Review of progress in shape-memory polymers," *J. Mater. Chem.*, vol. 17, no. 16, pp. 1543–1558, 2007. Accessed: Jan. 24, 2019. doi: 10.1039/b615954k.
[18] *Alien Technologies: The Higgs 3 SOT EPC Class 1 Gen 2 RFID Tag IC*. Accessed: Mar. 20, 2018. [Online]. Available: http://www.alientechnology.com/wp-content/uploads/ALC-360-SOT%20Higgs-3%20SOT%20(2016-11-03).pdf
[19] T. Bjorninen, M. Lauri, L. Ukkonen, R. Ritala, A. Z. Elsherbeni, and L. Sydanheimo, "Wireless measurement of RFID IC impedance," *IEEE Trans. Instrum. Meas.*, vol. 60, no. 9, pp. 3194–3206, 2011.
[20] D. Griffiths, *Introduction to Electrodynamics*. 4th ed. Cambridge, U.K.: Cambridge Univ. Press, 2017, p. 106.
[21] D. Pozar, *Microwave Engineering*, 4th ed. Hoboken, NJ, USA: Wiley, 2011, p. 78.
[22] M. Bolic, D. Simplot-Ryl, and I. Stojmenović, *RFID Systems*, 1st ed. Hoboken, NJ, USA: Wiley, 2010.
[23] G. Marrocco, "The art of UHF RFID antenna design: Impedance-matching and size-reduction techniques," *IEEE Antennas Propag. Mag.*, vol. 50, no. 1, pp. 66–79, Feb. 2008.
[24] H. Raihani, A. Benbassou, M. El Ghzaoui, and J. Belkadid, "Performance evaluation of a passive UHF RFID tag antenna using the embedded T-Match structure," in *Proc. Int. Conf. Wireless Technol., Embedded Intell. Syst. (WITS)*, Apr. 2017, pp. 1–6.
[25] X. Qing and Z. N. Chen, "Characteristics of a metal-backed loop antenna and its application to a high-frequency RFID smart shelf," *IEEE Antennas Propag. Mag.*, vol. 51, no. 2, pp. 26–38, Apr. 2009.
[26] N. A. Mohammed, K. R. Demarest, and D. D. Deavours, "Analysis and synthesis of UHF RFID antennas using the embedded T-match," in *Proc. IEEE Int. Conf. RFID (IEEE RFID)*, Orlando, FL, USA, Apr. 2010, pp. 230–236.
[27] T. White and D. Broer, "Programmable and adaptive mechanics with liquid crystal polymer networks and elastomers," *Nature Mater.*, vol. 14, pp. 1087–1098, Oct. 2015. Accessed: Aug. 24, 2018. doi: 10.1038/nmat4433.
[28] C. Modes, K. Bhattacharya, and M. Warner, "Disclination-mediated thermo-optical response in nematic glass sheets," *Phys. Rev. E, Stat. Phys. Plasmas Fluids Relat. Interdiscip. Top.*, vol. 81, no. 6, Jun. 2010, Art. no. 060701.
[29] C. Balanis, *Antenna Theory*, 3rd ed. Hoboken, NJ, USA: Wiley, 2005.
[30] G. González, *Microwave Transistor Amplifiers*, 2nd ed. Upper Saddle River, NJ, USA: Prentice-Hall, 1996, p. 47.
[31] P. V. Nikitin, K. V. S. Rao, S. F. Lam, V. Pillai, R. Martinez, and H. Heinrich, "Power reflection coefficient analysis for complex impedances in RFID tag design," *IEEE Trans. Microw. Theory Techn.*, vol. 53, no. 9, pp. 2721–2725, Sep. 2005.
[32] R. Meys and F. Janssens, "Measuring the impedance of balanced antennas by an S-parameter method," *IEEE Antennas Propag. Mag.*, vol. 40, no. 6, pp. 62–65, Dec. 1998.
[33] X. Qing, C. K. Goh, and Z. N. Chen, "Impedance characterization of RFID tag antennas and application in tag co-design," *IEEE Trans. Microw. Theory Techn.*, vol. 57, no. 5, pp. 1268–1274, May 2009.
[34] X. Qing, C. K. Goh, and Z. N. Chen, "Measurement of UHF RFID tag antenna impedance," in *Proc. IEEE Int. Workshop Antenna Technol.*, Santa Monica, CA, USA, Mar. 2009, pp. 1–4.
[35] (2018). *Agilent De-embedding and Embedding S-Parameter Networks Using a Vector Network Analyzer*. Accessed: Aug. 20, 2018. [Online]. Available: http://web.doe.carleton.ca/~nagui/labequip/loadpull/papers/sparams/Agilent_AN1364_S-parameter_De-embedding.pdf
[36] X. Yi, T. Wu, Y. Wang, and M. M. Tentzeris, "Sensitivity modeling of an RFID-based strain-sensing antenna with dielectric constant change," *IEEE Sensors J.*, vol. 15, no. 11, pp. 6147–6155, Nov. 2015.
[37] Atecorp.com. (2019). *Model SAS-571 Double Ridge Guide Horn Antenna*. Accessed: Jun. 21, 2019. [Online]. Available: https://www.atecorp.com/ATECorp/media/pdfs/data-sheets/AH-Systems-SAS-571_Datasheet.pdf
[38] N. Burt, N. Finney, and J. Young. (2018). *Fringe Field of Parallel Plate Capacitor*. Accessed: Jun. 19, 2018. [Online]. Available: http://srjcstaff.santarosa.edu/~yataiiya/UNDER_GRAD_RESEARCH/Fringe%20Field%20of%20Parallel%20Plate%20Capacitor.pdf
[39] S. Caizzone, C. Occhiuzzi, and G. Marrocco, "Multi-chip RFID antenna integrating shape-memory alloys for temperature sensing," in *Proc. 5th Eur. Conf. Antennas Propag. (EUCAP)*, Rome, Italy, Apr. 2011, pp. 2810–2813.
[40] Rrtcadd.org. (2019). *Water Amounts in Fruits and Vegetables*. Accessed: Jan. 12, 2019. [Online]. Available: http://rrtcadd.org/resources/Advocacy/Water-Amounts-in-Fruits-and-Vegetables—Handout-Week-10.pdf
[41] Slideshare.net. (2019). *Packing of Harvested Fruits and Vegetables*. Accessed: Jan. 12, 2019. [Online]. Available: https://www.slideshare.net/GayaniRasangika/packing-of-harvested-fruits-and-vegetables
[42] H. Saghlatoon, L. Sydänheimo, L. Ukkonen, and M. Tentzeris "Optimization of inkjet printing of patch antennas on low-cost fibrous substrates," *IEEE Antennas Wireless Propag. Lett.*, vol. 13, pp. 915–918, 2014.
[43] K. Blattenberger. (2019). *Dielectric Constant, Strength, & Loss Tangent—RF Cafe*. Accessed Jan. 12, 2019. [Online]. Available: http://www.rfcafe.com/references/electrical/dielectric-constants-strengths.htm

Yousuf Shafiq (S'13) received the B.S. and M.S. degrees in electrical engineering from Florida International University (FIU), Miami, FL, USA, in 2009 and 2010, respectively, where he is currently pursuing the Ph.D. degree in electrical engineering.

From 2010 to 2012, he was a Communications Systems Engineer with Lockheed Martin Space Systems, Newtown, PA, USA. Subsequently, he was a RCS Engineer at Pratt and Whitney, West Palm Beach, FL, USA. Finally, from 2014 to 2017, he was an Electrical Engineer with the Naval Surface Warfare Center, Panama City Beach, FL, USA. He is currently a Research Assistant with the RFCOM Lab, FIU. His current research interests include wireless sensing using innovative reactive materials combined with novel antenna and RF circuit design techniques.

John S. Gibson (M'11) received the B.S. degree in computer engineering from Bethune Cookman University, Daytona Beach, FL, USA, in 2013, and the Ph.D. degree in electrical and computer engineering from Florida International University (FIU), Miami, FL, USA, in 2018.

From 2013 to 2018, he was a Research Assistant with the ElectroMagnetics Lab, FIU. He joined the Air Force Research Laboratory (AFRL) Co-Op Pathways Program in 2016, and became a Full-Time Electronics Engineer with the Sensors Directorate, Wright Patterson Air Force Base, OH, USA, in 2018. He has authored or coauthored numerous conference papers. His current research interests include electro-optics for countermeasures sensors.

Dr. Gibson is a member of several professional societies. He was a recipient of the National Science Foundation Florida Georgia Louis Strokes Alliance Minority Program Bridge to Doctorate Fellowship in 2013 and the Florida Education Fund McKnight Doctoral in 2014.

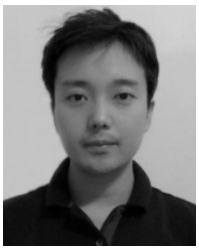

Hyun Kim received the B.S. degree in bioengineering and the M.S. degree in chemical engineering from the Inha University of South Korea, Incheon, South Korea, in 2010 and 2015, respectively.

He was an Engineer with the SK Chemicals, South Korea, focusing on pharmaceutical materials. His M.S. research was focused on multifunctional polymer composites. In 2015, he joined the Ware Group, The University of Texas at Dallas, Richardson, TX, USA, as a Ph.D. Student of biomedical engineering to study liquid crystal elastomer for actuator and electronic applications.

Cedric P. Ambulo received the B.A. degree in physics from Austin College, Sherman, TX, USA, in 2016.

He joined the Ware Research Lab, The University of Texas at Dallas, Richardson, TX, USA, in 2016. He is currently researching and developing stimuli-responsive, liquid crystal elastomer actuators toward soft robotic applications.

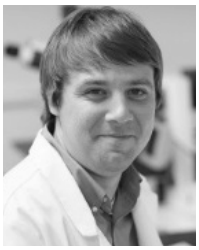

Taylor H. Ware received the B.S. degree from the Georgia Institute of Technology, Atlanta, GA, USA, in 2009, and the M.S. and Ph.D. degrees from The University of Texas at Dallas, Richardson, TX, USA, in 2011 and 2013, respectively.

From 2013 to 2015, he was a Post-Doctoral Researcher with the Air Force Research Laboratory, Wright Patterson Air Force Base, OH, USA. Since 2015, he has been an Assistant Professor with the Bioengineering Department, The University of Texas at Dallas. His current research interests include liquid crystal materials, flexible electronics, and biomaterials.

Stavros V. Georgakopoulos (S'93–M'02–SM'11) received the Diploma degree in electrical engineering from the University of Patras, Patras, Greece, in 1996, and the M.S. and Ph.D. degrees in electrical engineering from Arizona State University (ASU), Tempe, AZ, USA, in 1998, and 2001, respectively.

From 2001 to 2007, he was a Principal Engineer with SV Microwave, Inc., West Palm Beach, FL, USA. Since 2007, he has been with the Department of Electrical and Computer Engineering, Florida International University, Miami, FL, USA, where he is currently a Professor, the Director of the Transforming Antennas Center (a research center on foldable/origami, physically reconfigurable and deployable antennas), and the Director of the RF Communications, Millimeter-Waves, and Terahertz Lab. His current research interests include novel antennas, arrays, RFID, microwave and RF systems, novel sensors, and wireless powering of portable, wearable, and implantable devices.

Dr. Georgakopoulos received the 2015 FIU President's Council Worlds Ahead Faculty Award, which is the highest honor FIU extends to a faculty member for excelling in research, teaching, mentorship, and service. He has been serving as an Associate Editor for the IEEE TRANSACTIONS ON ANTENNAS AND PROPAGATION since 2013.